Deterministic Particle Assembly on Nanophotonic Chips

Razie Khalesi Moghaddam,[†] Nikhil Bhalla,[‡,¶] Amy Q.Shen,[§] and Giovanniantonio Natale[*,†]

[†]*Department of Chemical & Petroleum Engineering, University of Calgary, 2500 University Drive NW, Calgary, T2N 1N4, Alberta, Canada*

[‡]*Nanotechnology and Integrated Bioengineering Centre (NIBEC), School of Engineering, Ulster University, Shore Road, BT37 0QB Jordanstown, Northern Ireland, United Kingdom*

¶*Heathcare Technology Hub, Ulster University, BT37 0QB Jordanstown, Northern Ireland, United Kingdom*

§*Micro/Bio/Nanofluidics Unit, Okinawa Institute of Science and Technology Graduate University, Onna, Okinawa, Japan*

E-mail: gnatale@ucalgary.ca

Abstract:

Hypothesis: Controlled particle assembly from a dilute suspension droplet is challenging yet important for many lab-on-a-chip and biosensing applications. The formation of hot spots on the localized surface plasmonic resonance (LSPR) substrates induced by laser excitation can generate microbubbles. These microbubbles, upon the laser removal, shrink and collapse due to electron energy dissipation, leading to guided particle assembly on the LSPR substrate.

Experiments: After depositing dilute silica particles dispersions on both nanoisland (AuNI) and planar gold (Au) plasmonic substrates (referred to as LSPR and SPR substrates respectively), microbubbles were formed when a laser beam was applied. Particle dispersion concentration, laser power, and the radius of circular laser sequence were varied to produce different sizes of particle clusters on the LSPR substrate after bubble shrinkage upon the laser removal. To stabilize the assembled structures over time, sodium chloride (NaCl) was added to the dispersions.

Findings: Even though thermo-plasmonic flow and microbubbles can be produced with SPR substrates, particle assembly is only possible on LSPR substrates because of electron energy dissipation via nanoscale air gaps trapped in the LSPR substrate. By tuning the laser power, the radius of the circular laser sequence, and the particle dispersion concentration, the number of particles in the assembled structure can be controlled. The addition of NaCl to the dispersion can screen the

electrostatic charges among the particles and between the particles and substrate, favoring hydrogen bonding and stabilizing the assembled structures for hours. These findings establish a new framework for utilizing nanophotonic chips where particle assembly can be achieved by a single source of light.

Keywords: self-assembly, surface plasmonic resonance, nanophotonic chips, bubble shrinkage, hot spot formation

1. Introduction

The autonomous organization of particles into ordered structures is commonly known as the process of particle assembly [1] The ordered structures of particles exhibit unique collective properties, which has received great attention in diverse fields such as sensors [2], bioassays [3], photonic devices [4], high-density data-storage materials [5] and in the development of optical and electrical switches [6]. In particular, methods which assist particle assembly of microscale entities, such as colloidal particles, cells or single cell-organism, on top of solid substrates, has led to the development of advanced microfluidic chips where controlled handling of fluids and particles can be achieved [7-9].This has extended capabilities of microfluidic chips in various applications from use in bioassays and sensing systems [8],[10-14] to the development of new materials such as photonic papers [15] and colorless inks for colored writing applications [16].

Existing procedures to initiate on-chip self-assembly of particles are mainly based on the principles which exploit colloidal epitaxy [17], magnetic and electrodynamic force fields [18-20] to manipulate particles inside the microfluidic chips. While these forces can be well controlled to provide a reduced timescale of self-assembly inside a microfluidic chip, such methods are heavily dependent on the physical and chemical state (such as the charge and magnetic spin) of the particles and the suspension media, which limits their applicability to serve as a general method for particle assembly. Recently, techniques based on the acoustic forces demonstrated micro-particle self-assembly by overcoming the dependence of particle assembly methods on particle's electromagnetic properties [21, 22]. However, the acoustic force-based methods for the particle assembly completely rely on the particle accumulation at the pressure nodes inside the standing acoustic wave, making it heavily dependent on limits of acoustic wave generators. For example, to form a standing wave field the energy that is fed into the experimental chamber should be equal to its natural frequency.

Apart from the aforementioned magnetic, electrodynamic and acoustic mechanisms for particle assembly, capillary [23-25] and depletion force driven particle self-assembly [26, 27] and DNA

hybridization [28, 29] are other methods that can yield ordered structures. Although, these methods employ simple laboratory facilities, but special type of the particles in case of shape and surface modification is required to achieve desired result. Utilizing optical tweezers [30], tailored microfluidic channels based on either laminar flow [31] or Langmuir–Blodgett compression [32] can also organize microparticles. However, these techniques require additional components to enable sensor integration, which can increase the cost of the system, and they lack the ability to precisely control the number of particles in the assembled clusters. Moreover, they often require complex microchannel designs specific to the particle size/type. For instance, the chips which use laminar flow for the particle assembly are limited by the flow rates [33] within the microchannels or the physical device dimensions. Phase separation induced self-assembly of anisotropic colloidal particle is also reported in literature [34, 35]. However, most of these studies imply that particle suspension needs to be mono-dispersed and sufficiently concentrated for particles to arrange themselves in assembled structures. Therefore, new methodologies for particle assembly, which are independent of device, particle properties, and suspension concentrations, while providing precise control on the number of particles assembled in clusters, are required to develop new processing schemes for advanced material with controlled microstructures.

In this context, we demonstrate here how micro-particles can be assembled on nanophotonic substrates, utilizing localized surface plasmon resonance (LSPR) phenomenon: when a light beam is introduced at an interface of a metal nanostructure and a dielectric (such as air, water, etc.), free electrons of the metal start oscillating at a specific wavelength [36]. This leads to a strong near field energy localization on the top metal nanostructures, further creating hot spots (spots with increased temperature) *via* the process of thermoplasmonic effects [37-40]. To initiate self-assembly of particles, hot spots are first generated in the LSPR substrates using a laser beam which creates microbubbles in the solution resting on top of the metal nanostructures of the LSPR substrate, inducing a thermal convective flow [7, 41-43]. As a result, the particles within the solution are brought into contact at the bubble interface [41, 43]. Once particles reach the bubble surface, they are trapped because of the balance between surface tension and the pressure forces that are dominant in the system compared to the drag forces. Upon removal of laser beam, the energy of electrons in the hot spots quickly dissipates, leading to a quick shrinkage of the bubble which assists in the particle cluster formation on the LSPR substrates. This facilitates formation of assembled cluster of micro-particles on a simple experimental setup and even at dilute concentration regime (where occasional collisions between particles can be ignored). We observe that this quick

shrinkage of the micro-bubble is absent in the SPR substrates, where micro-bubbles are found to be stable for hours after the laser removal, suggesting that the feature of particle assembly and subsequent cluster formation is exclusive to the LSPR substrates. Most importantly, the particle cluster size, size and the location of the microbubble on the LSPR substrate can be controlled by changing the laser power and beam location, size of the sequential illumination path, and initial particle concentration, thereby achieving deterministic assembly of micro-particles on the nanophotonic chips.

2. Experimental section

2.1. LSPR and SPR substrate fabrication

Both gold nanoisland (AuNI) and planar gold (Au) plasmonic substrates are fabricated using borosilicate glasses and gold. Note that the AuNI and Au substrates, are referred to as LSPR and SPR substrates respectively. To develop nanostructured LSPR substrates, Au film of 4 nm thickness is first deposited on the glass, followed by the annealing step at 560°C for 3 hours to generate AuNI distributed across the glass substrate. For the SPR substrate, 30 nm of Au film is deposited on the glass. The deposition of gold on all glass substrates is performed using electron beam vapor deposition equipment (KE604TT1-TKF1, Kawasaki Science) in a class 1000 clean room. Prior to the gold deposition, the glass substrates are sonicated in acetone for 5 minutes, followed by thorough rinsing in isopropanol to remove acetone stains and drying used compressed air.

2.2. Particle dispersions

Non-porous silica particle of 3.17 μm in diameter are purchased from Bangs Laboratories, Inc., USA. To prepare particle dispersion, a desired mass of particles is dispersed in deionized water (H_2O) by sonication. Five dispersions with the concentration of 0.01, 0.02, 0.04, 0.06 and 0.10 g/L are prepared and used in the experiments. All these concentrations are in dilute concentration regime (volume fraction < 5% for spherical particles) where particles do not interact with each other. Moreover, in order to stabilize the assembled structures over time, a dispersion of 0.10 g/L of particles in a 1 M NaCl solution is used.

2.3. Hot spot generation

The hot spots are generated by a laser beam (Tweez 300i, Aresis) which illuminates either a single or

series of spots on the LSPR substrate. A continuous wave infrared laser beam (5000 mW, 1064 nm) passes through an acousto-optic deflector (AOD) to achieve millisecond control on the position of the laser beam. The beam is expanded using a beam expander before it enters the microscope (Nikon, Ti2 Eclipse, Japan). The expanded beam is combined with the optical pathway of the microscope by a dichroic mirror. When the beam reaches the sample cell, it can produce hot spots in the desired location. The experimental images are captured by a CMOS camera. Utilizing the AOD, the position of the optical spot and the strength of the laser can be controlled [44]. This optical set-up also enables us to design a sequence of illuminated points instead of a single point. The laser beam is switched on the specified points with a frequency of 50 kHz. This allows us to create a sequence of hot spots onto the substrate. A schematic of the sequential laser illumination is provided in the supplementary information. The results presented in this work are based on 10 μm circular sequences to generate bubbles of 60-80 μm in diameter. Sequences with different diameters are also used to see the effect of the size of sequential illumination on the final size of the particle clusters.

2.4. Characterization and analysis

Scanning electron microscopy (SEM) is used to characterize the size and morphology of the SPR (planar gold) and and LSPR (AuNI) substrates. A section of the plasmonic substrate is cut from the original sample using a diamond-tipped glass cutter and attached to a scanning electron microscope (SEM, FEI Quanta 250 FEG) mount using carbon tapes. SEM measurements are taken between 5 and 30 eV to obtain high-resolution images with magnification of at least 100,000X. The average diameter and island-to-island distance of AuNI are obtained by using the particle analysis module in ImageJ software. The AuNI are assumed to be circular and bright in the image with threshold type processing. The detailed morphology of AuNI are analyzed after applying a contrast threshold with three independent images. The extinction spectrum of LSPR and SPR substrates is acquired using UV-Vis- NIR (Ultra Violet-Visble-Near InfraRed) spectroscopy performed using CRAIC Technologies microspectrometer suite.

3. Results and Discussion

Planar and nanostructured surfaces of SPR (Au) and LSPR (AuNI) substrates respectively, are fabricated to understand if the particle assembly phenomenon described in this work is exclusively due to thermoplasmonic effects or due to combinatorial effects of geometry and plasmons. Fundamentally, both SPR and LSPR exhibit collective oscillation of electrons, except that in LSPR

substrates the size of nanostructures absorbing light is smaller than the wavelength of light absorption. Figure 1 a and b show the top view of the LSPR and SPR substrates. The LSPR substrate is composed of island-like spherical structures in contrast to a continuous planar gold film in the SPR substrate. Figure 1 c and d show the normalized extinction of LSPR and SPR substrates in the UV-Visible (300-750 nm), and the NIR (750-2000 nm) of the spectrum. While the fundamental plasmonic resonance peak for both type of substrates are observed within visible region, typical for Au planar and nanostructured surfaces [36] (see figure 1 c), we can also clearly see that there is an extinction of photon energy at 1064 nm (see figure 1 d), which is the wavelength of the laser used in this work. Note that this extinction at 1064 nm, Au of 0.71 a.u. & AuNI of 0.22 a.u. (see dotted line within figure 1 d), should not be confused with the strong LSPR, SPR resonance mode absorbances, similar to the one observed in the visible regime of the light spectrum. These broad wavelength extinctions can be attributed to 1) weak plasmonic modes which exists within the Au material- as also seen between 1050-1060 nm in the literature [45, 46]; 2) quasi homogenous distribution AuNI in the case of LSPR substrates which leads to inhomogeneous broadening of plasmonic absorbances [47, 48]; and 3) inherent metal reflections within Au films in the infrared region [49]. Nevertheless, these combinatorial effects will give rise to hot spots within the LSPR substrate and an elevated film temperature of SPR substrate at the solid-liquid interface [50, 51]. In addition, we find that the mean diameter of the AuNI is 19.68 nm, see Figure 1e, with the average aspect ratio (major axis: minor axis, where ratio of 1 indicates a perfect circle) of 1.28, see Figure 1 f, suggesting that the AuNI are quasi spherical in shape.

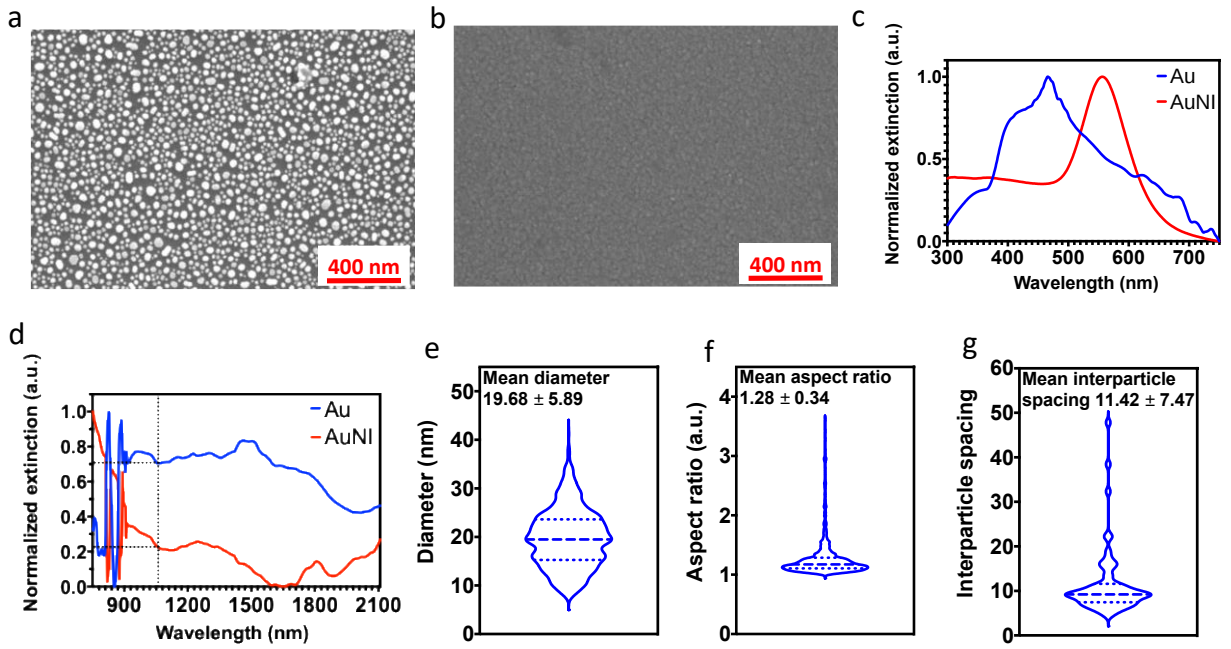

Figure 1*: SEM images of a) gold nanoislands (AuNI) and b) the top surface of gold film with thickness of 20 nm. Both SEM images are acquired at 10,000 X magnification; The extinction spectrum of the Au film and AuNI substrates c) in the UV-Vis region of the spectrum, and d) in the NIR region (dotted line is guide to extinction values at 1064 nm); Morphological features of the AuNI substrate where e) shows the average diameter, f) aspect ratio, and g) interparticle spacing between the AuNI.*

The mean interparticle distance is 11.42 nm as shown in Figure 1 g. These morphological features of AuNI are typical to the Au island based LSPR substrates by using the dewetting process for biosensing applications [52]. A distinct extinction peak is observed around 545 nm (Figure 1c), validating the LSPR nature of the substrate.

3.1. Particle manipulation and assembly on LSPR substrates

We next demonstrate that using LSPR substrates in combination with the infrared energy excitation to generate microbubbles is an efficient way to manipulate particles and induce particle self-assembly even in the dilute concentration regime. Figures 2a and b show an example of how the diameter of a microbubble evolves over time, generated on the LSPR and SPR substrate, respectively. Here the concentration of the micro-particle dispersion is 0.04 g/L (in the dilute concentration regime). A 10 μm circular laser sequence (sequential illumination of the substrate with laser beam on a specific path is called laser sequence) was used to generate the microbubbles on both substrates. The bubbles formed on the LSPR substrates eventually collapse after the laser

removal. In contrast, the bubbles formed on SPR substrates keep growing for a few hours even after the laser removal. Shrinkage of microbubbles formed on LSPR substrates is ascribed to the structural discontinuity in the AuNI substrates which isolates the energy dissipation associated with the plasmons on the LSPR substrates, upon removal of the laser power.

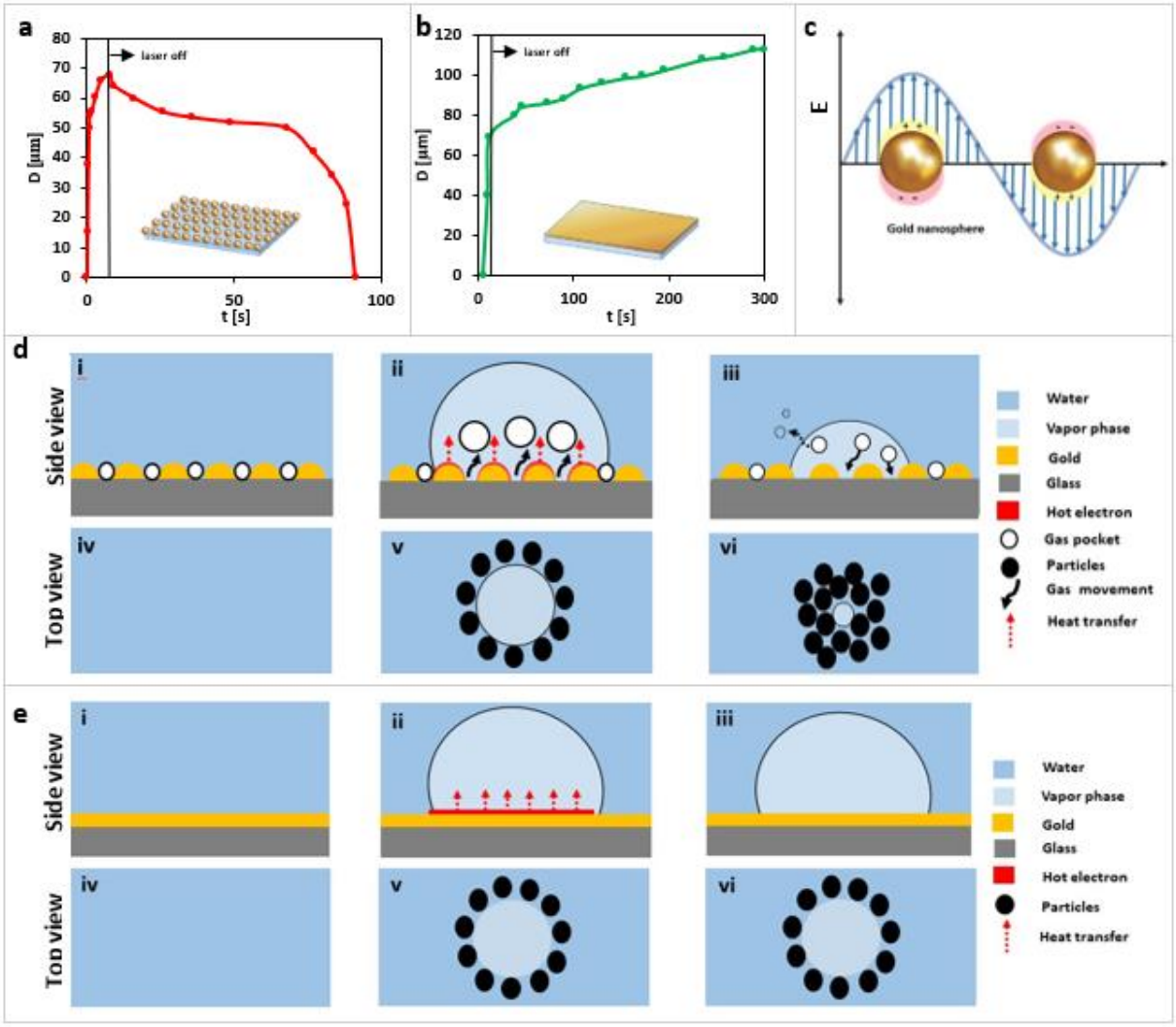

***Figure 2**: Microbubble diameter changes with respect to time on a) a typical LSPR substrate (effective laser power: 5 W). b) a typical SPR substrate (effective laser power: 0.50 W). In both cases the laser was removed after 10 seconds. c) Schematic of surface plasmons formation in the presence of light. Schematic explaining the mechanism of micro-bubble formation on d) LSPR substrates, e) SPR substrates. The particle size, concentration of the dispersion and the size of the laser sequence used in the experiments associated with a) and b) are 3.17 µm, 0.04 g/L and 10 µm, respectively.*

A schematic showing how plasmons are formed on LSPR substrates is illustrated in Figure 2c. In comparison, on SPR substrates, the thermoplasmonic heat dissipation is inefficient due to the structural continuity of Au films. In these SPR substrates, plasmons are distributed over the

surface of the substrate and because Au regions are continuous (unlike LSPR nanoisland substrates) the dissipation of the energy is slow. Therefore, even when the laser is turned off, one can observe a slow radiative decay. As a result, the bubbles keep growing after removing the laser for a few hours until all the heat is dissipated. Moreover, the power needed to form the bubble in the case of the planar Au substrate is 10 times lower than the LSPR substrate. This is again attributed to the continuous energy loss in the AuNI due to the interparticle spacing present in the LSPR substrates which creates nanoscale air pockets between adjacent Au nanostructures. Generally, there are two possible mechanisms behind the micro-bubble formation on the AuNI substrates: expansion of the air bubbles present in the water phase or vaporization of the water at its boiling point. As degassing of the solutions does not affect the formation of the bubbles (see more details in supplementary information), the expansion of the air cavities in the water can be ruled out as the reason behind the bubble formation (consistent with previous literature) [41, 42]. In addition, previous reports suggest that some air can be trapped inside the nanostructures [53, 54] and upon heating this trapped air can be released into the solution. This mechanism is illustrated in Figure 2 d i-vi (LSPR substrate) and Figure 2 e i-vi (SPR substrates).

Upon the laser removal, the air is released from the micro-bubble (it returns to the interisland spaces or dissolves in the water) which leads to a fast shrinkage of bubbles on the LSPR substrate (see schematic in Figure 2d i-vi) as compared to the SPR substrate (see schematic in Figure 2e i-vi). In both sub figures, i-iii represent the cross-sectional view of the substrates and iv-vi represent the top view of the bubble corresponding to the conditions shown in Figure 2a and b. Bubble shrinkage, unique to the LSPR substrate, is caused by the dissipation of energy which is more prominent in LSPR substrates. When the LSPR substrate is illuminated by the laser, the electrons are excited and oscillated around the Au atoms (figure 2c). Returning the electrons to their initial state cause heating due to non-radiative surface plasmon decay [36]. In the LSPR case, the spaces between the islands make the radiative decay very weak. The generated heat can heat up the water and expand the cavities resulting in the bubble formation. When the laser is turned off, the hot Au atoms start to cool down via conduction through Au-glass slide interface and Au-liquid interface and initiate the condensation. Because the amount of heated gold mass in the LSPR substrate are less than SPR one, the cooling process would be easier. While in the SPR case, the generated heat can distribute over the surface through conduction via Au-Au atoms, heat up the Au atoms that are in contact

with the water and maintain the water for the longer time in the gaseous state. In addition, in the SPR substrate we have a higher number of electrons that are excited, then the heat that they generated is higher and last longer [18, 55].

While the laser is applied, local heating of the AuNIs determines simultaneously the formation of the bubble and a thermal convective flow towards the center of the bubble [41-43]. If the particles are freely present in the solution, they will move towards the bubble and eventually be trapped at the interface of the bubble. This sink-like flow triggers colloidal cluster formation even at ultralow particle concentrations (far from phase transition concentrations) after shrinkage of the bubble upon laser removal. A captured time sequence of this process is shown in Figure 3 a-f, for the case of the LSPR substrate where the particles trapped at the bubble surface eventually form a colloidal cluster after the bubble collapses. The irregular shape of the final cluster originates from the pressure wave caused by Brownian motion of particles upon condensation of the bubble. These results show that LSPR substrate is potentially an appropriate choice for the cluster formation due to bubble shrinkage while this feature is absent in the SPR substrate. Note that in Figure 3 we used 0.04 g/L as the concentration of micro-particle dispersion.

3.2. Mechanism of cluster formation

The laser creates a hot spot on the AuNIs, generating a temperature gradient in the liquid suspension while the bubble forms and grows because of the solvent evaporation. Distances far away from the bubble interface and considering stokes flow, the velocity field magnitude decays as $|u| \sim O(1/r)$ and neglecting the particle inertia, the motion of the particles can be described by a simple balance of forces:

$$F_D + F_T + F_B = 0, \quad (1)$$

where F_D is the drag force, F_T is the thermophoretic force, and F_B is the Brownian force. Note that we neglect gravity that does not contribute in the direction of motion of the particles (the gravity is acting in the z direction). In our system F_D completely dominates the other two forces. Specifically, the Peclet number in our experiments $P_e = \frac{(6\pi\mu a^2 v)}{K_B T}$, representing the ratio between flow and Brownian time scales, is ~O(10^2) where v is the magnitude of the particle velocity, a is the particle diameter, μ is the solvent viscosity, and K_BT is the thermal energy product of the Boltzmann constant, K_B, and the absolute temperature T.

Moreover, the thermophoretic velocity of silica particles in water (in the condition similar to our experiments) was reported[56] to be on the order of 10^{-6} m/s which is one order of magnitude lower than the translational velocity of the particles in our experiments $\sim 2 \times 10^{-5} m/s$. Once the particle reaches the interface, the particle is able to overcome the pressure of the bubble and absorb to the interface. However, the Marangoni flow is not sufficient to overcome gravity. The magnitude of the Marangoni flow velocity, v_M, moving against the gravity direction (direction z) can be estimated as $v_M \sim \left| \frac{\frac{d\gamma}{dT}\frac{\partial T}{\partial z}R}{\mu} \right| \sim 10^{-8}\ \frac{m}{s}$ where $\frac{d\gamma}{dT}$ is the water surface tension gradient with respect to temperature (0.17 mN/m.K for our experiments), and R is the radius of the bubble [57]. The ratio between the drag force generated by this velocity ($6\pi\mu a^2 v_M$) and the gravity force acting on the particles ($\frac{4}{3}\pi a^3 \rho_p g$ where ρ_p is the density of the particle and g is gravitational acceleration) is $\sim O(10^{-1})$. Hence, the particles tend to accumulate at the contact line of the substrate and the bubble interface. The particles, now pinned at interface, follow the bubble during the condensation process and eventually form a cluster once the bubble collapses.

3.3. Effect of the laser power

To study the effect of the laser power, we keep the dispersion concentration at 0.04 g/L while applying a 10 μm circular laser sequence on the LSPR substrate. The rates of expansion and decay of the bubbles are shown in Figure 4a, b and c. The rate of expansion grows with increasing laser power. Due to the concentration of higher amount of energy in the Au nanostructures, the generated bubbles expand faster when the laser power increases. Upon the laser removal, Figure 2a depicts the decay of the bubbles with two stages: initially slow followed by a fast shrinkage stage (decay rates shown in Figure 4b and c). In both cases the rate of decay increases with increasing laser power. When the laser power is higher, more energy is delivered to the Au nanostructures, therefore a stronger temperature gradient is formed, which results in a much faster heat transfer between the substrate and the surrounding media, further leading to a faster shrinkage of bubbles in the 2nd decay stage. At the same time, during bubble shrinkage, condensation of the water phase and thermal diffusion determines the rate of shrinkage of the bubble. It is important to note that the energy dissipation due to the condensation process scales with R^3 while the energy flux related to thermal diffusion scales with R^2.

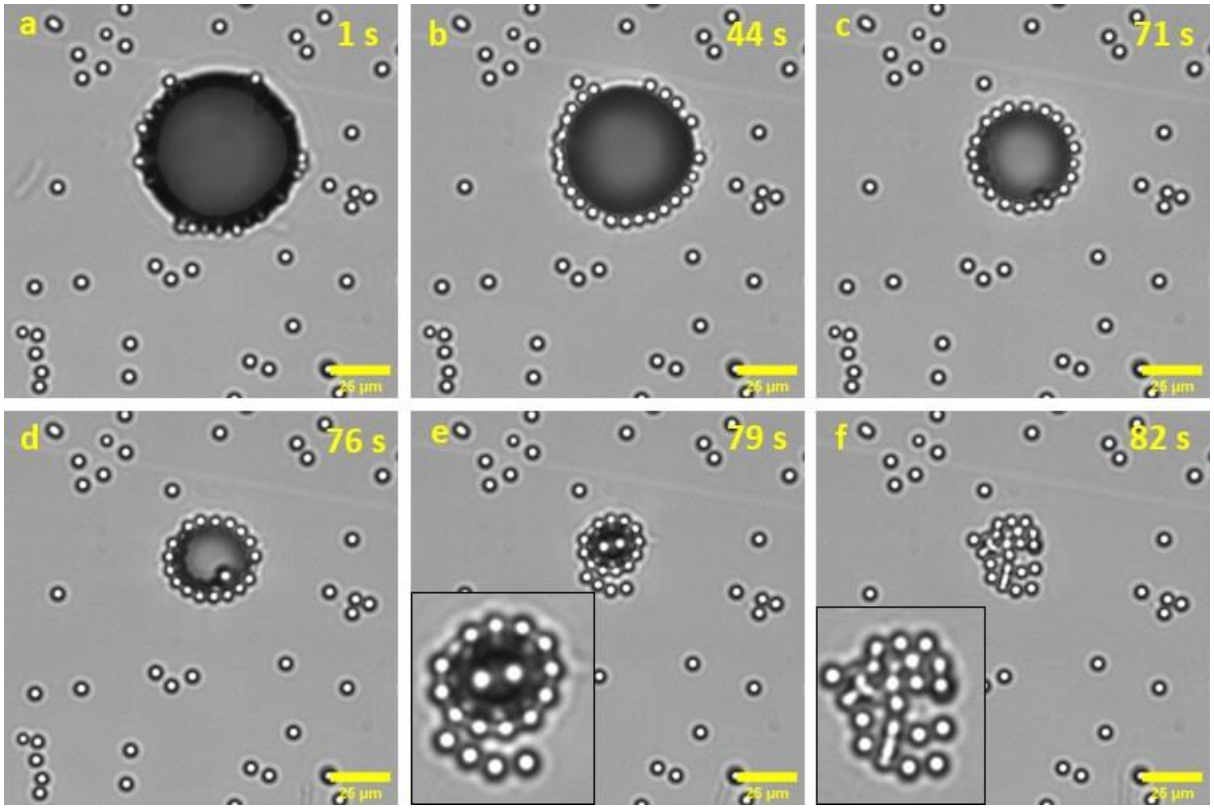

***Figure 3**: The decay of the bubble radius upon the laser removal. The pictures are captured at: a) 1s, b) 44s, c) 71s, d) 76s, e)79s, f) 82s after removing the laser beam. The scale bar is 20 µm. The concentration of the dispersion and the size of the laser sequence used in these experiments were 0.04 g/L and 10 µm respectively.*

Hence, condensation dominates at large radii until thermal diffusion becomes more important at smaller radii. Unfortunately, this simple model is not sufficient to predict the two slopes measured experimentally because the energy equation is complicated by the plasmonic energy dissipation, but it still provides a rationale behind the two slopes captured

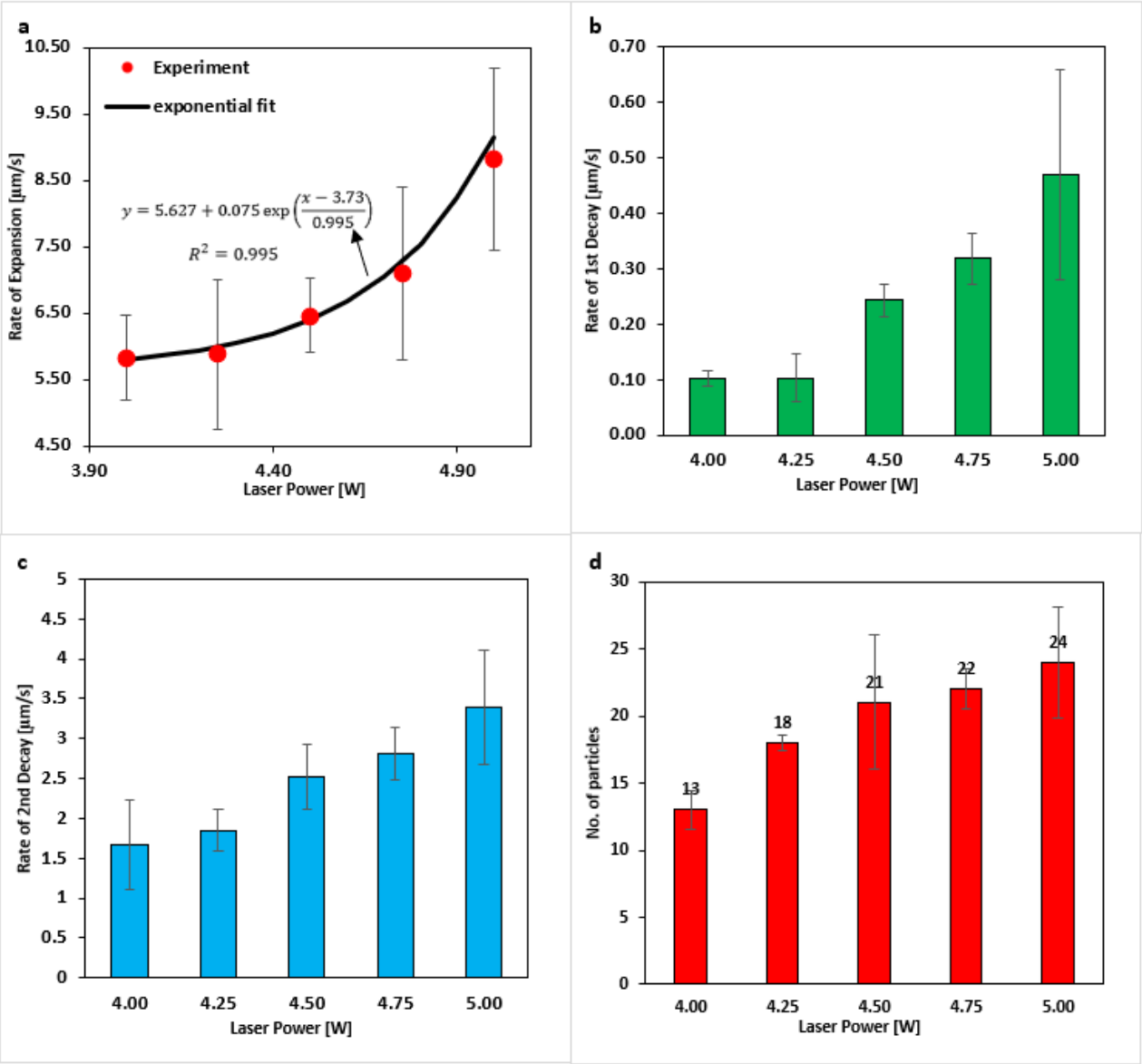

***Figure 4**: Effect of the laser power on a) the rate of expansion when laser is active, b) rate of the first decay and c) rate of the second decay after removing the laser, d) size of the final cluster of particles formed on LSPR substrates using a 10 µm circular laser sequence. The concentration of the dispersion and the size of the laser sequence used in these experiments are 0.04 g/L and 10 µm respectively.*

experimentally. In addition, when the laser power is higher, the number of particles collected at the bubble interface is also higher because of the enhanced convective flows towards the hot spot. On the other hand, the size of the bubble slightly increases with the increasing laser power. This provides a larger interfacial area for the particles to reside on the circumference of the bubble. The possibility of changing laser power and forming bubbles with different sizes gives us the ability to form clusters with different number of particles as shown in Figure 4d.

3.4. Effect of the circular sequence size

Considering the direct correlation between the size of the microbubble and the size of the final particle cluster, we explore the possibility to generate microbubbles with various diameters by applying different sizes of laser beam spot/sequences. Illuminating the LSPR substrate sequentially in a specific path leads to the formation of tiny bubbles (less than 10 microns) beyond the boundaries of the circular path illuminated by the laser beam spots. These microbubbles merge instantaneously and form a larger bubble with a size bigger than the laser illumination spot. Therefore, by defining circular sequences with various diameters, we can form microbubbles of different sizes. This feature of our method enables us to interrogate and form bubbles over large area of the nanostructures within the LSPR substrate. This suggests that by simply changing the size of the laser sequence, the number of particles being trapped at the surface can be adjusted. Figure 5 shows an example of the evolution of the diameter of the generated bubble and the final size of the particle cluster versus the size of the applied laser sequence. It is observed that larger laser sequence results in larger bubbles, which allows higher number of particles to be assembled around the bubbles on this LSPR substrate. This trend is observed for the laser sequences having sizes up to 12 μm. When a sequence with a laser sequence size of 15 μm is used, even though the size of the resulting bubble is larger, the number of particles in the cluster is reduced. This is because the path of the illuminating laser becomes sufficiently large which slows down the merging of the tiny bubbles. During the formation of the tiny bubbles and their merging, the particles in the solution have enough time to get trapped at the interface of the microbubbles. These particles are expelled out from the interface of the microbubble during the merging process. Hence, they do not return to the interface of the final bubble because of the large separation distance from it (see supplementary information). The inset shows the particle coverage ([number of particles*particle diameter]/[π*bubble diameter]) for different sizes of laser beam sequences. The particle coverage scatters around 1.0 for the sequences with the diameters less than 15 μm implying that the particles fully cover the contact line. Consistently, the particle coverage for the laser sequence with the size of 15 μm drastically decreases to 0.65 because of the above-mentioned particle expulsion mechanism. Note that in figure 5 the zero circular sequence diameter implies the application of the laser beam in a single spot.

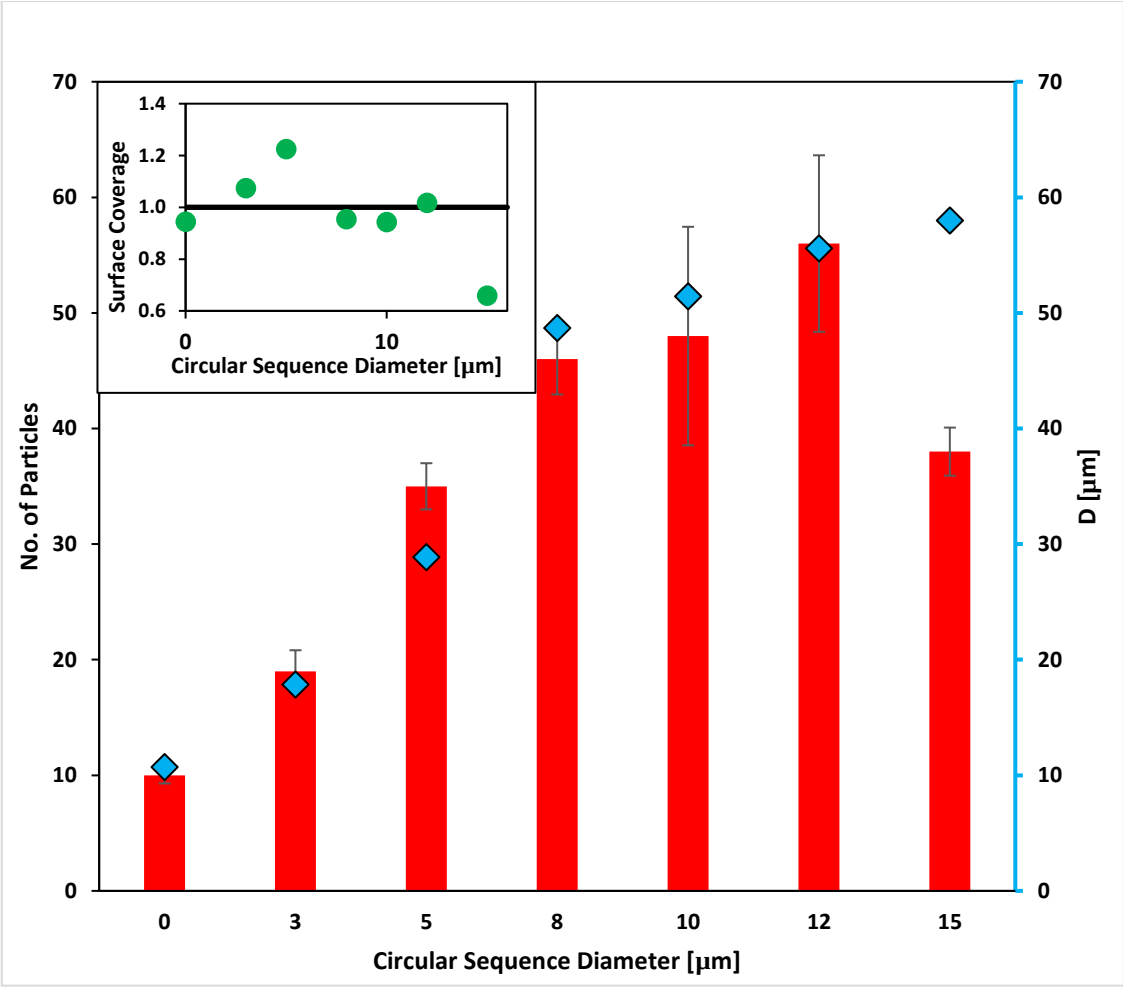

Figure 5: The effect of the size of the laser sequence on the size of the generated bubbles (blue diamonds) and the number of particles present in the clusters (red columns). The laser power was set at 5 W and the concentration of the dispersion was 0.10 g/L. Inset shows the surface coverage of the bubble vs different sizes of the laser sequence.

3.5. Effect of the dispersion concentration

Figure 6 shows the effect of dispersion concentration (0.01, 0.02, 0.04, 0.06 and 0.10 g/L) on the number of particles formed in a cluster with five concentrations. Note that all concentrations fall under the dilute concentration regime. Keeping the size of the generated bubble constant (which is resulted from constant laser power and the laser sequence size), the final size of the cluster increases with increasing dispersion concentration.

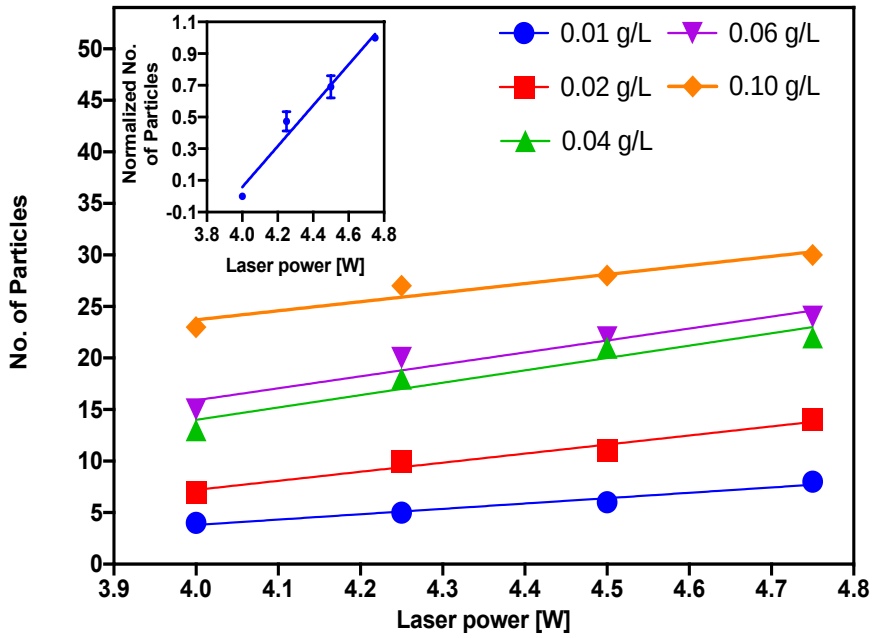

Figure 6*: The effect of laser power on the number of particles assembled for different concentration of particle dispersion. The inset shows normalized number of particles versus the laser power to highlight the fact that the number of particles increase with increase in the laser power. All lines represent linear regression fit within the* $R^2 > 0.98$*. Note that 10 µm circular laser sequence was used in this experiment to generate the bubbles.*

The thermal convective sink-like flows can swipe a larger number of particles around the bubble that are trapped at the interface. As a result, after the bubble shrinkage, the final size of the particle cluster is larger at higher dispersion concentrations. Figure 6 illustrates that this trend is consistent for a range of laser power in our experiments, with the inset showing that the normalized number of particles (number of particles in each cluster/maximum number of particles) increases with increasing laser power. We can determine the number of particles which can be assembled within a cluster by simple tuning of the concentration of the particles or/and the power of laser. This is valuable in cases where a specific number of particles are required to achieve a desire level of properties to design processing schemes for advanced material manufacturing.

3.6. Cluster stabilization

To demonstrate the capability of our methodology to generate self-assembled structure, we demonstrate here stable cluster formation via addition of NaCl salt. The clusters formed by silica particles are stable only for a few minutes because of Brownian motion and electrostatic repulsion forces. Specifically, the negative charge on the silica particles (-85 mV [58]) and the gold substrate

(-35 mV [59]) implies repulsive particle-particle and particle-substrate forces which lead to short-time stability of the formed structures. Addition of salt to the dispersion screens the surface charges of particles and gold nanoparticles reducing the electrical double layer length. Consequently, hydrogen bonding is favored between particles and particle-substrate that stabilizes the assembled structures for hours (the maximum observation time was of 5 hours). Figure 7 shows the number of particles in each cluster versus change in the laser sequence size in the presence of a monovalent salt (1M). Micrographs of the stable clusters obtained with the different circular sequences are reported in Figure S3 in the supplementary information. However, the addition of salt reduces the dimension of the clusters when compared to the dimension of the clusters in the figure 6. The hydrogen bonding interactions between particles and the substrate reduces the particle motion resulting in less number of particles being transported to the bubble interface via thermal convection. The produced bubbles are able to collect particles and trap them at their interfaces from a distance of few particle diameters near their circumferences.

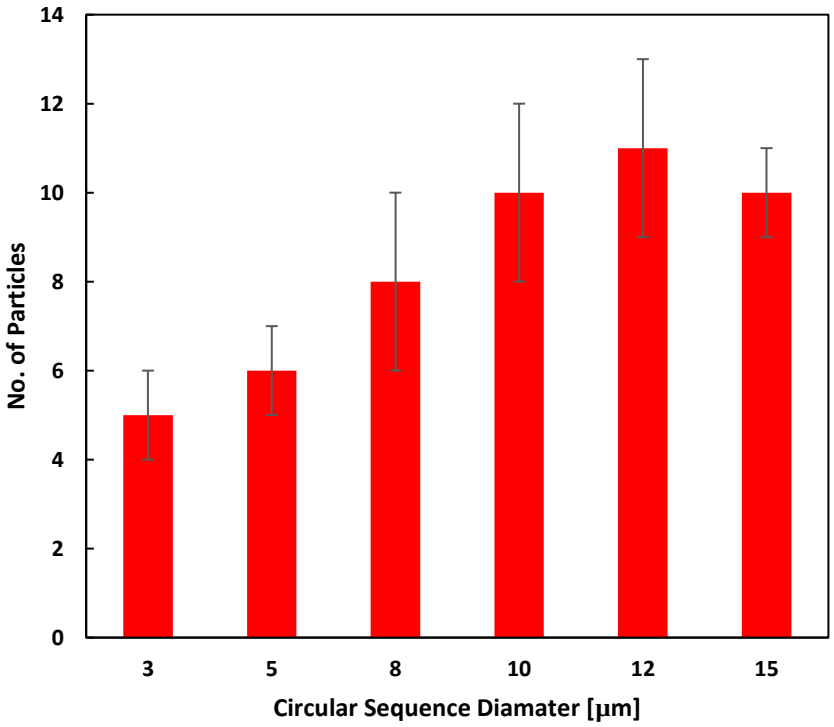

Figure 7*: The effect of the size of the laser sequence on the final size of the clusters of particles in the presence of NaCl ions. The laser power was set at 5 W and the concentration of the dispersion was 0.10 g/L.*

4. Significance of the method:

Self-assembly of colloidal micron size particle is conducted through a nanophotonic self-asembly method. The results provided in the previous sections showed that clusters with different size in any arbitrary position on the LSPR substrate is easily and quickly accessible. To obtain the particle clusters no particle surface treatment and no specific geometry of particles are required. In addition, the method provides the capability of particle cluster formation in dilute regime of concentrations. In table 1 some of these features are compared with some of other available methods of particle self-assembly reported in the literature.

Table 1 *Comparison of features of currently available particle self-assembly methods.*

Requirements	**Depletion force driven method [26, 27, 60, 61]**	**Capillary force driven method [23-25, 62, 63]**	**Magnetic and electric field driven methods [64-67]**	**DNA hybridization [28, 29, 68, 69]**	**Flow field driven method [70-73]**	**Acoustic field driven method [21, 22, 74, 75]**	**Nanophotonic self-assembly**
Specific particle Geometry	No	Rod like is preferred	No	No	No	No	No
Particle surface modification	No	No	Yes	Yes	No	No	No
Presence of other additives	yes	Yes	No	Yes	No	No	No
Specific instrumentation	No	No	Yes	No	Yes	Yes	Yes
Outcomes							
Control of position of clusters	No	Yes	No	No	No	Yes	Yes
Control of cluster size	No	No	Yes	No	No	No	Yes
Cluster stability at standard ambient conditions	Yes	Yes	No	No	No	No	Yes

5. Conclusions

The ordered structure of particles exhibits unique collective properties that has received great attention in different fields [2-6]. Numerous methods have been proposed in the literature to assemble particles in clusters or crystals [17, 18, 21, 23, 26, 28, 30]. However, these methodologies do not achieve control on number of particles in the clusters and position of clusters during self-assembly. This is a requirement to generate new processes and materials [76, 77]. In this study, a flexible and robust approach for the guided assembly of the silica particles was demonstrated based on shrinkage of the bubbles with sizes ranged between 10-100 microns being generated by hot spots on

the LSPR substrates. Using a simple laser beam, bubbles with different sizes were produced and served as a template for controlled assembly of particles around the plasmonic hot spot. After removing the laser, the shrinkage of the bubble led to particle cluster formation. Various laser powers and sizes of sequential laser illumination were assessed to study the bubble size and to control the final size of the cluster. Increasing the laser power and the size of the sequences led to the formation of clusters with a larger number of particles. The particle dispersion concentration was found as another effective variable to control the size of the final particle cluster such that with the increase in the dispersion concentration, the final size of the cluster increased. The assembled structures could be maintained over time when salt was added to the dispersion. Our approach coupling LSPR with unique laser sequences is extremely flexible: particle surface modification is not required, and it has the potential to be used for a wide range of particles. Moreover, our approach can be used to control particle assemblies where a specific number of particles is required to achieve the desired level of local properties. As summarized in Table 1, this level of control in cluster size and position and the ability to form multiple clusters as desired makes the proposed methodology an innovative solution overcoming many of the limitations of other self-assembly approaches available in the literature. Other than the flexibility of the method to form the clusters, formation of large arrays of particles on the LSPR substrates, can improve the overall precision and detection fidelity where these substrates are used as sensors.

Acknowledgements

R.K. and G.N. acknowledge the support of the Canada First Research Excellence Fund (CFREF) and of the Natural Sciences and Engineering Research Council of Canada (NSERC), [funding reference number 03783]. A.Q.S. acknowledges the support of the Okinawa Institute of Science and Technology Graduate University (OIST) with subsidy funding from the Cabinet Office, Government of Japan. A.Q.S also acknowledges funding from the Joint Research Projects (JRPs) supported by JSPS and SNSF. Authors would like to thank Mr. Kang-Yu Chu from OIST for his help with SEM imaging.

References

1. Malaquin, L., et al., *Controlled particle placement through convective and capillary assembly.* 2007. **23**(23): p. 11513-11521, https://doi.org/10.1021/la700852c.

2. Holtz, J.H. and S.A.J.N. Asher, *Polymerized colloidal crystal hydrogel films as intelligent chemical sensing materials.* 1997. **389**(6653): p. 829-832, https://doi.org/10.1038/39834.

3. Uspal, W.E., H.B. Eral, and P.S.J.N.c. Doyle, *Engineering particle trajectories in microfluidic flows using particle shape.* 2013. **4**(1): p. 1-9, https://doi.org/10.1038/ncomms3666.

4. Lopez, C.J.A.M., *Materials aspects of photonic crystals.* 2003. **15**(20): p. 1679-1704, https://doi.org/10.1002/adma.200300386.

5. Gourevich, I., et al., *Multidye nanostructured material for optical data storage and security labeling.* 2004. **16**(8): p. 1472-1479, https://doi.org/10.1021/cm030070f.

6. Kumar, S., F. Maury, and N.J.S.r. Bahlawane, *Electrical Switching in Semiconductor-Metal Self-Assembled VO 2 Disordered Metamaterial Coatings.* 2016. **6**(1): p. 1-13, https://doi.org/10.1038/srep37699.

7. Ryu, K., S.K. Chung, and S.K.J.J.J.o.t.A.f.L.A. Cho, *Micropumping by an acoustically excited oscillating bubble for automated implantable microfluidic devices.* 2010. **15**(3): p. 163-171, https://doi.org/10.1016%2Fj.jala.2010.01.012.

7. Yue, T., et al., *On-chip self-assembly of cell embedded microstructures to vascular-like microtubes.* 2014. **14**(6): p. 1151-1161, https://doi.org/10.1039/C3LC51134K.

8. Lee, W., et al., *Dynamic self-assembly and control of microfluidic particle crystals.* 2010. **107**(52): p. 22413-22418, https://doi.org/10.1073/pnas.1010297107.

9. Rosenbluth, M.J., W.A. Lam, and D.A.J.L.o.a.C. Fletcher, *Analyzing cell mechanics in hematologic diseases with microfluidic biophysical flow cytometry.* 2008. **8**(7): p. 1062-1070, https://doi.org/10.1039/B802931H.

10. Xu, X., et al., *Microfluidic single-cell Omics analysis.* 2020. **16**(9): p. 1903905, https://doi.org/10.1002/smll.201903905.

11. Nasiri, R., et al., *Microfluidic-Based Approaches in Targeted Cell/Particle Separation Based on Physical Properties: Fundamentals and Applications.* 2020. **16**(29): p. 2000171, https://doi.org/10.1002/smll.202000171.

12. Guzniczak, E., et al., *Deformability-induced lift force in spiral microchannels for cell separation.* 2020. **20**(3): p. 614-625, https://doi.org/10.1039/C9LC01000A.

13. Khetani, S., et al., *Engineering shelf-stable coating for microfluidic organ-on-a-chip using bioinspired catecholamine polymers.* 2020. **12**(6): p. 6910-6923, https://doi.org/10.1021/acsami.9b20826.

14. Guidetti, G., et al., *Photonic paper: Multiscale assembly of reflective cellulose sheets in Lunaria annua.* 2020. **6**(27): p. eaba8966, https://doi.org/10.1126/sciadv.aba8966.

15. Fudouzi, H. and Y.J.A.M. Xia, *Photonic papers and inks: color writing with colorless materials.* 2003. **15**(11): p. 892-896, https://doi.org/10.1002/adma.200304795.

16. van Blaaderen, A. and P. Wiltzius, *Growing large, well-oriented colloidal crystals*. 1997, Wiley Online Library, https://doi.org/10.1002/adma.19970091015.

17. Yeh, S.-R., M. Seul, and B.I.J.N. Shraiman, *Assembly of ordered colloidal aggregrates by electric-field-induced fluid flow.* 1997. **386**(6620): p. 57-59, https://doi.org/10.1038/386057a0.

18. Swan, J.W., et al., *Directed colloidal self-assembly in toggled magnetic fields.* 2014. **10**(8): p. 1102-1109, https://doi.org/10.1039/C3SM52663A.

19. Aizenberg, J., P.V. Braun, and P.J.P.r.l. Wiltzius, *Patterned colloidal deposition controlled by electrostatic and capillary forces.* 2000. **84**(13): p. 2997, https://doi.org/10.1103/PhysRevLett.84.2997.

20. Destgeer, G., et al., *Microparticle self-assembly induced by travelling surface acoustic waves.* 2019. **9**(14): p. 7916-7921, https://doi.org/10.1039/C8RA09859J.

21. Oh, J.S., G.-R. Yi, and D.J.J.A.n. Pine, *Reconfigurable Self-Assembly and Kinetic Control of Multiprogrammed DNA-Coated Particles.* 2020. **14**(4): p. 4595-4600, https://doi.org/10.1021/acsnano.0c00164.

22. Brinker, C.J., et al., *Evaporation-induced self-assembly: nanostructures made easy.* 1999. **11**(7): p. 579-585, https://doi.org/10.1002/(SICI)1521-4095(199905)11:7%3C579::AID-ADMA579%3E3.0.CO;2-R.

23. Lao, Z., et al., *Capillary force driven self-assembly of anisotropic hierarchical structures prepared by femtosecond laser 3D printing and their applications in crystallizing microparticles.* 2015. **9**(12): p. 12060-12069, https://doi.org/10.1021/acsnano.5b04914.

24. Duan, H. and K.K.J.N.L. Berggren, *Directed self-assembly at the 10 nm scale by using capillary force-induced nanocohesion.* 2010. **10**(9): p. 3710-3716, https://doi.org/10.1021/nl102259s.

25. Kraft, D.J., et al., *Surface roughness directed self-assembly of patchy particles into colloidal micelles.* 2012. **109**(27): p. 10787-10792, https://doi.org/10.1073/pnas.1116820109.

26. Galanis, J., R. Nossal, and D.J.S.M. Harries, *Depletion forces drive polymer-like self-assembly in vibrofluidized granular materials.* 2010. **6**(5): p. 1026-1034, https://doi.org/10.1039/B918034F.

27. Moon, J., et al., *DNA-Coated Microspheres and Their Colloidal Superstructures.* 2018. **26**(12): p. 1085-1094, https://doi.org/10.1007/s13233-018-6151-8.

28. Melde, K., et al., *Acoustic fabrication via the assembly and fusion of particles.* 2018. **30**(3): p. 1704507, https://doi.org/10.1002/adma.201704507.

29. Van Rosmalen, M.G., et al., *Revealing in real-time a multistep assembly mechanism for SV40 virus-like particles.* 2020. **6**(16): p. eaaz1639, https://doi.org/10.1126/sciadv.aaz1639.

30. Wu, Z., et al., *Controllable synthesis of multicompartmental particles using 3D microfluidics.* 2020. **132**(6): p. 2245-2249, https://doi.org/10.1002/ange.201911252.

31. Grillo, F., et al., *Self-templating assembly of soft microparticles into complex tessellations.* 2020. **582**(7811): p. 219-224, https://doi.org/10.1038/s41586-020-2341-6.

32. Dendukuri, D., et al., *Continuous-flow lithography for high-throughput microparticle synthesis.* 2006. **5**(5): p. 365-369, https://doi.org/10.1038/nmat1617.

33. van der Kooij, F.M., K. Kassapidou, and H.N.J.N. Lekkerkerker, *Liquid crystal phase transitions in suspensions of polydisperse plate-like particles.* 2000. **406**(6798): p. 868-871, https://doi.org/10.1038/35022535.

34. Luo, M., et al., *Size-dependent ultraviolet luminescence and low-field electron emission of TiO2 nanodots formed by phase-separation-induced self-assembly.* 2009. **42**(10): p. 105414, https://doi.org/10.1088/0022-3727/42/10/105414.

35. Willets, K.A. and R.P.J.A.R.P.C. Van Duyne, *Localized surface plasmon resonance spectroscopy and sensing.* 2007. **58**: p. 267-297, https://doi.org/10.1146/annurev.physchem.58.032806.104607.

36. Palermo, G., et al., *Flexible thermo-plasmonics: An opto-mechanical control of the heat generated at the nanoscale.* 2018. **10**(35): p. 16556-16561, https://doi.org/10.1039/C8NR04228D.

37. Xue, B., et al., *Towards high quality triangular silver nanoprisms: improved synthesis, six-tip based hot spots and ultra-high local surface plasmon resonance sensitivity.* 2015. **7**(17): p. 8048-8057, https://doi.org/10.1039/C4NR06901C.

38. Zhang, Y., et al., *Full-visible multifunctional aluminium metasurfaces by in situ anisotropic thermoplasmonic laser printing.* 2019. **4**(3): p. 601-609, https://doi.org/10.1039/C9NH00003H.

39. Lereu, A.L., et al., *Thermoplasmonic shift and dispersion in thin metal films.* 2008. **26**(4): p. 836-841, https://doi.org/10.1116/1.2900713.

40. Zhao, C., et al., *Theory and experiment on particle trapping and manipulation via optothermally generated bubbles.* 2014. **14**(2): p. 384-391, https://doi.org/10.1039/C3LC50748C.

41. Zheng, Y., et al., *Accumulating microparticles and direct-writing micropatterns using a continuous-wave laser-induced vapor bubble.* 2011. **11**(22): p. 3816-3820, https://doi.org/10.1039/C1LC20478E.

42. Chikazawa, J.-i., et al., *Flow-induced transport via optical heating of a single gold nanoparticle.* 2019. **123**(7): p. 4512-4522, https://doi.org/10.1021/acs.jpcc.8b11575.

43. Song, H., et al., *Study of in vitro RBCs membrane elasticity with AOD scanning optical tweezers.* 2017. **8**(1): p. 384-394, https://doi.org/10.1364/BOE.8.000384.

44. Li, A., et al., *Engineering the hot spots in squared arrays of gold nanoparticles on a silver film.* 2016. **8**(34): p. 15658-15664, https://doi.org/10.1039/C6NR03692A.

45. Fayaz, A.M., et al., *Vancomycin bound biogenic gold nanoparticles: A different perspective for development of anti VRSA agents.* 2011. **46**(3): p. 636-641, https://doi.org/10.1016/j.procbio.2010.11.001.

46. Nehl, C.L., et al., *Scattering spectra of single gold nanoshells.* 2004. **4**(12): p. 2355-2359, https://doi.org/10.1021/nl048610a.

47. Machida, K. and K.J.J.o.A.P. Adachi, *Particle shape inhomogeneity and plasmon-band broadening of solar-control LaB6 nanoparticles.* 2015. **118**(1): p. 013103, https://doi.org/10.1063/1.4923049.

48. Trollmann, J. and A.J.T.J.o.P.C.C. Pucci, *Infrared dielectric function of gold films in relation to their morphology.* 2014. **118**(27): p. 15011-15018, https://doi.org/10.1021/jp5027465.

49. Nguyen, S.C., et al., *Study of heat transfer dynamics from gold nanorods to the environment via time-resolved infrared spectroscopy.* 2016. **10**(2): p. 2144-2151, https://doi.org/10.1021/acsnano.5b06623.

50. Carlomagno, G.M. and G.J.E.i.f. Cardone, *Infrared thermography for convective heat transfer measurements.* 2010. **49**(6): p. 1187-1218, https://doi.org/10.1007/s00348-010-0912-2.

51. Bhalla, N., et al., *Dual-mode refractive index and charge sensing to investigate complex surface chemistry on nanostructures.* 2017. **9**(2): p. 547-554, https://doi.org/10.1039/C6NR07664E.

52. Baffou, G., et al., *Super-heating and micro-bubble generation around plasmonic nanoparticles under cw illumination.* 2014. **118**(9): p. 4890-4898, https://doi.org/10.1021/jp411519k.

53. Belova, V., et al., *Influence of adsorbed gas at liquid/solid interfaces on heterogeneous cavitation.* 2013. **4**(1): p. 248-256, https://doi.org/10.1039/C2SC21321D.

54. Lapotko, D.J.N., *Plasmonic nanoparticle-generated photothermal bubbles and their biomedical applications.* 2009. **4**(7): p. 813-845, https://doi.org/10.2217/nnm.09.59.

55. Regazzetti, A., M. Hoyos, and M.J.T.J.o.P.C.B. Martin, *Experimental evidence of thermophoresis of non-Brownian particles in pure liquids and estimation of their thermophoretic mobility*. 2004. **108**(39): p. 15285-15292, https://doi.org/10.1021/jp031321a.

56. Fujii, S., et al., *Fabrication and placement of a ring structure of nanoparticles by a laser-induced micronanobubble on a gold surface.* 2011. **27**(14): p. 8605-8610, https://doi.org/10.1021/la201616s.

57. Xu, G., J. Zhang, and G.J.P.t. Song, *Effect of complexation on the zeta potential of silica powder*. 2003. **134**(3): p. 218-222, https://doi.org/10.1016/S0032-5910(03)00172-4.

58. Lung, J.-K., et al., *Preparation of gold nanoparticles by arc discharge in water*. 2007. **434**: p. 655-658, https://doi.org/10.1016/j.jallcom.2006.08.213.

59. Kumar, S., et al., *Block-copolymer-induced long-range depletion interaction and clustering of silica nanoparticles in aqueous solution.* 2013. **87**(4): p. 042315, https://doi.org/10.1103/PhysRevE.87.042315.

60. Zhang, J., et al., *Synthesis and self-assembly of squarelike PbCrO4 nanoplatelets via micelle-mediated depletion attraction.* 2013. **29**(15): p. 4679-4687, https://doi.org/10.1021/la4001347.

61. Hu, Y., et al., *Laser printing hierarchical structures with the aid of controlled capillary-driven self-assembly*. 2015. **112**(22): p. 6876-6881, https://doi.org/10.1073/pnas.1503861112.

62. Morris, C.J., B.A.J.J.o.M. Parviz, and Microengineering, *Micro-scale metal contacts for capillary force-driven self-assembly*. 2007. **18**(1): p. 015022, https://doi.org/10.1088/0960-1317/18/1/015022.

63. Lumsdon, S.O., E.W. Kaler, and O.D.J.L. Velev, *Two-dimensional crystallization of microspheres by a coplanar AC electric field.* 2004. **20**(6): p. 2108-2116, https://doi.org/10.1021/la035812y.

64. Promislow, J.H. and A.P.J.L. Gast, *Magnetorheological fluid structure in a pulsed magnetic field.* 1996. **12**(17): p. 4095-4102, https://doi.org/10.1021/la960104g.

65. Zhang, L. and Y.J.L. Zhu, *Directed assembly of janus particles under high frequency ac-electric fields: Effects of medium conductivity and colloidal surface chemistry*. 2012. **28**(37): p. 13201-13207, https://doi.org/10.1021/la302725v.

66. Yan, J., et al., *Linking synchronization to self-assembly using magnetic Janus colloids.* 2012. **491**(7425): p. 578-581, https://doi.org/10.1038/nature11619.

67. Biancaniello, P.L., A.J. Kim, and J.C.J.P.r.l. Crocker, *Colloidal interactions and self-assembly using DNA hybridization.* 2005. **94**(5): p. 058302, https://doi.org/10.1103/PhysRevLett.94.058302.

68. Knorowski, C., A.J.C.O.i.S.S. Travesset, and M. Science, *Materials design by DNA programmed self-assembly.* 2011. **15**(6): p. 262-270, https://doi.org/10.1016/j.cossms.2011.07.002.

69. Vermant, J. and M.J.J.o.P.C.M. Solomon, *Flow-induced structure in colloidal suspensions.* 2005. **17**(4): p. R187, https://doi.org/10.1088/0953-8984/17/4/R02.

70. Grzelczak, M., et al., *Directed self-assembly of nanoparticles.* 2010. **4**(7): p. 3591-3605, https://doi.org/10.1021/nn100869j.

71. Panine, P., et al., *Structure and rheology during shear-induced crystallization of a latex suspension.* 2002. **66**(2): p. 022401, https://doi.org/10.1103/PhysRevE.66.022401.

72. Stancik, E.J., et al., *Dynamic transitions and oscillatory melting of a two-dimensional crystal subjected to shear flow.* 2004. **48**(1): p. 159-173, https://doi.org/10.1122/1.1631425.

73. Collino, R.R., et al., *Acoustic field controlled patterning and assembly of anisotropic particles.* 2015. **5**: p. 37-46, https://doi.org/10.1016/j.eml.2015.09.003.

74. Sazan, H., et al., *Directed assembly of nanoparticles into continuous microstructures by standing surface acoustic waves.* 2019. **536**: p. 701-709, https://doi.org/10.1016/j.jcis.2018.10.100.

75. Zhang, R., et al., *Metal–Organic Framework Crystal-Assembled Optical Sensors for Chemical Vapors: Effects of Crystal Sizes and Missing-Linker Defects on Sensing Performances.* 2019. **11**(23): p. 21010-21017, https://doi.org/10.1021/acsami.9b05933.

76. Ajayaghosh, A. and V.K.J.A.o.C.R. Praveen, *π-Organogels of self-assembled p-phenylenevinylenes: soft materials with distinct size, shape, and functions.* 2007. **40**(8): p. 644-656, https://doi.org/10.1021/ar7000364.